Supplemental information

Electrocatalytic Nitrate Reduction to Ammonia with a Bifunctional Ni-Mo Alloy Catalyst

Miao Zhao,[ac] Ruizhi Duan,[ad] Zicong Zhang,[ac] Qi Mao,[a] Qingnan Wang,[a] Yiyang Zhou,[ac] Xun Wang,[a] Chunmei Ding[*abc] and Can Li[*ac]

[a] State Key Laboratory of Catalysis, Dalian National Laboratory for Clean Energy, Dalian Institute of Chemical Physics, Chinese Academy of Sciences, Dalian 116023, China. E-mail: canli@dicp.ac.cn; cmding@dicp.ac.cn

[b] Center of Materials Science and Optoelectronics Engineering, University of Chinese Academy of Sciences, Beijing 100049, China

[c] University of Chinese Academy of Sciences, Beijing 100049, China.

[d] Key Laboratory of Advanced Catalysis, Gansu Province, State Key Laboratory of Applied Organic Chemistry, College of Chemistry and Chemical Engineering, Lanzhou University, Lanzhou 730000 Gansu, China

Experimental section

Preparation and characterizations of catalysts

All reagents were purchased and used as received without further purification. All aqueous solution was prepared using ultrapure water (>18 MΩ). To remove the surface oxide species, Ni foams (thickness 2 mm, Guangshengjia New Materials) were ultrasonically cleaned by acetone (AR, 99.5%, Sinopharm Chemical Reagent), isopropyl alcohol (AR, 99.7%, Sinopharm Chemical Reagent) and 1 M HCl (AR, 36.0% ~ 38.0%, Kermel) solution for 15 min in turn, and subsequently rinsed with water and ethanol (AR, 99.7%, Sinopharm Chemical Reagent). The cleaned Ni foam was immersed into 30 mL aqueous solution containing 1.2 mmol $Ni(NO_3)_2 \cdot 6H_2O$ (AR, 98.0%, Sinopharm Chemical Reagent) and 0.8 mmol $Na_2MoO_4 \cdot 2H_2O$ (AR, 96%, Aladdin) in a Teflon-lined stainless autoclave (50 mL). The autoclave was sealed and treated in an oven at 150 ºC for 6 h. The resultant sample was cleaned by ultrasonic treatment for 1 min in water, washed with water and ethanol and finally dried at 60 ºC for 2 h in a vacuum oven. Then the sample was put into a quartz tube furnace and calcined at 550 ºC (heating rate 3 ºC min^{-1}) for 60 min under the mixed atmosphere of H_2 (30 sccm) and Ar (200 sccm). In the last step, the samples were electrochemically reduced at −0.52 V vs. RHE for 30 min in 1 M KOH before conducting NO_3RR. Finally, NiMo-1.2-0.8 ($Ni_{2.44}Mo$) was obtained. For NiMo-n-m, n mmol $Ni(NO_3)_2 \cdot 6H_2O$ and m mmol $Na_2MoO_4 \cdot 2H_2O$ was added during preparation.

All characterizations were conducted after the electrochemical reduction treatment otherwise stated. The morphology and element mapping of catalysts were characterized by SEM (scanning electron microscopy, Quanta 200 FEG) equipped with an EDX (energy dispersive spectroscopy). TEM (transmission electron microscope, HITACHI HT7700) and HRTEM (high resolution

transmission electron microscope) were used to study the lattice structure. XRD (X-ray diffraction) measurements were carried out on Rigaku D/Max-2500/PC under 40 kV and 200 mA using Cu Kα radiation. ESR spectra were tested on a Bruker A200 with DMPO (5,5-dimethyl-1-pyrroline-N-oxide) as the hydrogen radical trapping reagent.

Electrochemical measurements

Electrochemical measurements were carried out using an electrochemical workstation (CHI 1140C, Shanghai Chenhua) in an H-type cell separated by a FAA-PK-A30 membrane in 1 M KOH (AR, 85.0%, Sinopharm Chemical Reagent) with 0.5 M KNO_3 (AR, 99.0%, Kermel). The catalyst modified Ni foam, Ag/AgCl electrode (saturated KCl) and a Pt foil were used as the working electrode, reference electrode and counter electrode, respectively. The area of the working electrode was controlled to be 0.6*0.6 cm^2. NO_3RR was carried out by potentiostatic tests for 40 min with a stirring rate of 500 rpm in a water bath of 30 ºC, unless otherwise mentioned. The linear sweep voltammetry (LSV) curves were measured at a scan rate of 10 mV s^{-1}. Cyclic voltammetry (CV) curves for the determination of double-layer capacitance (C_{dl}) were measured in a none-Faradaic potential window at different scan rates in 1 M KOH. The plot of current density at a constant potential against scan rate has a linear relationship, and its slope is the C_{dl}. All potentials were recorded vs. RHE with *i*R compensation (80%) unless otherwise stated according to equation (1), where *i* is the measured current and *R* is the measured resistance.

$$E\ (RHE)_{corrected} = E\ (Ag/AgCl) + 0.197 + 0.059 \times pH - 80\%\ iR \quad (1)$$

Product analysis

NH_3 was determined using Nessler reagent (K_2HgI_4, Macklin) as the color reagent.[1] First, a certain amount of electrolyte was taken out from the electrolytic cell and diluted to 2 mL to the

detection range, and then neutralized with 2 mL 0.5 M H_2SO_4 solution. Next, 0.2 mL potassium sodium tartrate solution (1.5 M in water, Aladdin) was added and mixed thoroughly. Then, 1 mL Nessler reagent (Aladdin) was added into the solution, and then the solution was allowed to stand for 20 min. Finally, the absorbance at 425 nm was recorded. And the standard curve was detected using a series of standard NH_4Cl (AR, 99.5%, Kermel) solution.

The NO_2^- product was detected according to the Griess method.[2] Typically, the coloring agent was prepared by dissolving 10 mL H_3PO_4 (AR, 85%, Sinopharm Chemical Reagent), N-(1-naphthyl) ethyldiamine dihydrochloride (0.2 g, AR, 98%, Aladdin), and sulfonamide (4.0 g, 98%, Thermo Scientific) in 50 ml deionized H_2O. Then, 0.1 ml coloring agent was added into the liquid product (4.0 ml, neutralized with 2 mL 0.5 M H_2SO_4 solution), and the mixed solution was allowed to stand at room temperature for 15 min to generate a magenta azodye. Finally, the concentration of NO_2^- was determined by the absorbance at 540 nm.

Isotope labeling experiments

$K^{15}NO_3$ (99 at.%, Aladdin) was used as the feeding nitrogen source to perform the isotopic labeling experiments. The mixed solution of 1 M KOH and 0.1 M $K^{15}NO_3$ was added into the cathode and anode compartments. After reaction, electrolyte was taken out and the pH value was adjusted to be weak acid with 0.5 M H_2SO_4 for further quantification by ^{1}H-NMR (400 MHz) with external standard of dimethyl sulfoxide (DMSO).

Calculation of *r*(NH_3) and Faradaic efficiency (FE)

For NO_3RR, the $r(NH_3)$ was calculated by the equation (2):

$$r(NH_3) = Vc(NH_3) / tS \quad (2)$$

The FE was defined from the charge consumed for NH_3 production and total charge passed

through the electrode according to equation (3):

$$FE = nFc(NH_3)V / it \quad (3)$$

where V is the volume (10 mL) of electrolyte in the cathode compartment, t is the electrolysis time (40 min), S is the geometric area of working electrode (0.36 cm^2), $c(NH_3)$ is the generated concentration of NH_3, n is electron transfer number (8 for NO_3^- reduction to NH_3), F is the Faradaic constant (96485 C mol^{-1}), and i is average current.

DFT calculations

In this work, all DFT calculations were carried out with a periodic slab model using the Vienna *ab initio* simulation program (VASP 6.3.0).[3, 4] The interaction between the core and valence electrons was described using the frozen-core projector augmented wave (PAW) approach.[5, 6] The generalized gradient approximation (GGA) was used with the Perdew-Burke-Ernzerhof (PBE) exchange-correlation functional.[7] The energy cutoffs of 500 eV for plane wave functions were used for optimization and self-consistent calculations. A Gaussian smearing was used with a width of 0.1 eV for the relaxations and binding energy calculations of the reaction intermediates. The optimized geometries were fully relaxed until all atoms have Hellmann-Feynman forces lower than 0.02 eV $Å^{-1}$ and electronic iterations convergence less than 10^{-5} eV by Normal algorithm. Van der Waals correction of Grimme with zero-damping was used to improve the description of the dispersion interaction between adsorbates and substrates.[8]

The $4 \times 4 \times 1$ supercell of the Mo(111), Ni(111) and NiMo(133) facets with four atomic layers with the bottom two layers fixed was taken as the substrate model. That's because Mo(111) is the most stable facet of Mo, Ni(111) is the most stable facet of Ni, and NiMo(133) is the mainly exposed facet of NiMo alloy. A slab model with a vacuum layer of 15 Å was used to model the catalyst

surface. The Brillouin zone was sampled by the 3 × 3 × 1 Monkhorst-Pack k-point mesh for the total energy calculation. Minimum energy paths and corresponding activation barriers for all elementary steps were calculated using the climbing image-nudged elastic band approach (CI-NEB),[9] and we analyzed the stretching frequencies to characterize whether a stationary point is a minimum state without imaginary frequency or a transition state with only one imaginary frequency.

The reaction energetics as a function of the applied potential with the proton-electron pair are determined using the computational hydrogen electrode (CHE) method.[10] At pH = 0 in the electrolyte and 1 bar of H_2 in the gas phase at 298 K, the reaction free energy of 1/2 $H_2 = H^+ + e^-$ is zero at an electrode potential of $U = 0$.

The detailed reaction equations for the electrochemical NO_3RR route to yield NH_3 are presented below:

$$* + NO_3^- \rightarrow *NO_3 + e^-$$

$$*NO_3 + 2H^+ + 2e^- \rightarrow *NO_2 + H_2O$$

$$*NO_2 + 2H^+ + 2e^- \rightarrow *NO + H_2O$$

$$*NO + H^+ + e^- \rightarrow *NOH$$

$$*HNO + 2H^+ + 2e^- \rightarrow *NH_2OH$$

$$*NH_2OH + 2H^+ + 2e^- \rightarrow *NH_3 + H_2O$$

$$*NH_3 \rightarrow NH_3 + *$$

where * represents the active site. For each subsequent elementary step, the free energy is calculated after gas correction:

$$\Delta G_0 = \Delta E + \Delta E_{ZPE} - T\Delta S \quad (4)$$

where ΔE is the difference of electronic energy between products and reactants calculated using DFT.

ΔE_{ZPE} is the zero-point energy correction to the Gibbs free energy (estimated from frequency calculation). ΔS is the change in entropy for each reaction, and the entropy values of gaseous molecules and adsorbed molecules are calculated by VASPKIT (Vienna Ab-initio Simulation Package).[11] Room temperature (298.15 K) is used in the calculations to consider temperature influence.

To avoid directly computing the energy of charged NO_3^-, gaseous HNO_3 is used as a reference in the following steps.[12] Correspondingly, the adsorption energy of NO_3^- (ΔG_{*NO3}) can be approximately expressed as:

$$\Delta G_{*NO3} = G_{*NO3} - G^* - G_{HNO3}\,(g) + 0.5G_{H2}\,(g) + \Delta G_{correct}$$

$$\Delta G_{correct} = -\Delta G_{S1} - \Delta G_{S2}$$

where G_{*NO3}, G^*, G_{HNO3} (g) and G_{H2} are the Gibbs free energy of NO_3^- adsorption, HNO_3 and H_2 molecules in the gas phase, respectively. $\Delta G_{correct}$ denotes the correction of adsorption energy. According to CRC handbook of chemistry and physics, $\Delta G_{S1} = -0.075$ eV and $\Delta G_{S2} = -0.317$ eV. Therefore, $\Delta G_{correct}$ is set to 0.075 + 0.317 = 0.392 eV.

We include the effect of a bias on all states involving an electron in the electrode by shifting the energy of this state by $\Delta G_U = -eU$, where U is the electrode potential relative to the standard hydrogen electrode (SHE) potential. All NO_3RR pathway is calculated in 1 M KOH (pH = 14) at −0.14 V vs SHE, equivalent to 0.69 V_{RHE}. The free energy of H^+ is corrected by the concentration dependence of the entropy:

$$\Delta G_{pH}\,(pH) = -kT\cdot\ln[H^+] = kT\cdot\ln10\cdot pH$$

The reaction free energy is then calculated as: $\Delta G = \Delta G_0 + \Delta G_U + \Delta G_{pH}$

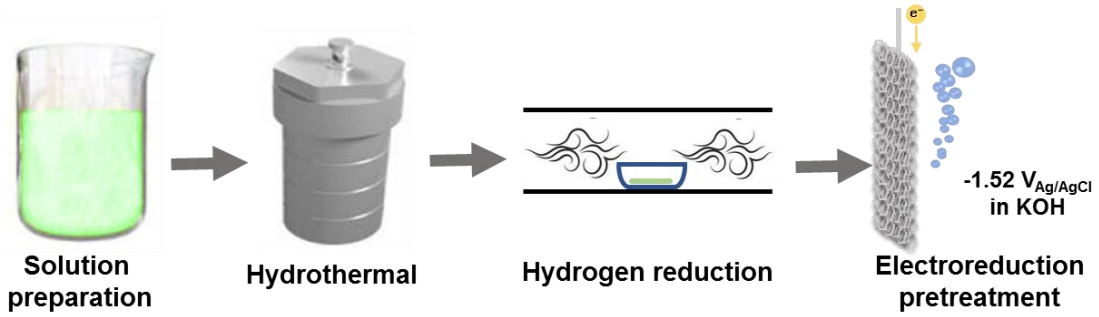

Fig. S1 Schematic illustration of the preparation of $Ni_{2.44}Mo$ on a Ni foam.

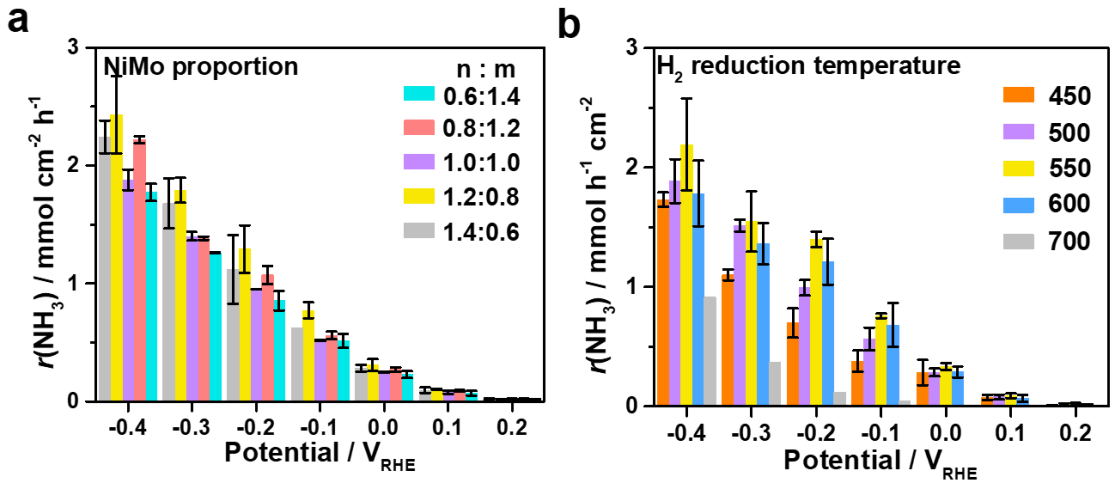

Fig. S2 Optimization of preparation conditions: **(a)** The activities of Ni-Mo catalysts prepared from n mmol of $Ni(NO_3)_2$ and m mmol of Na_2MoO_4 precursors. **(b)** The activities of NiMo-1.2-0.8 ($Ni_{2.44}Mo$) prepared at different temperatures of H_2 reduction.

Table S1 Atom ratios of NiMo-n-m samples prepared with n mmol $Ni(NO_3)_2$ and m mmol Na_2MoO_4 determined by EDX analysis of the catalyst particles peeled off from the substrate.

	NiMo-0.4-1.6	NiMo-0.8-1.2	NiMo-1.0-1.0	NiMo-1.2-0.8	NiMo-1.4-0.6	NiMo-1.6-0.4	NiMo-2-0
Ni:Mo	5.16	4.15	3.03	2.44	2.95	4.26	∞
Mo:Ni (Mo content relative to Ni)	19%	24.1%	33%	41%	34%	23.4%	0

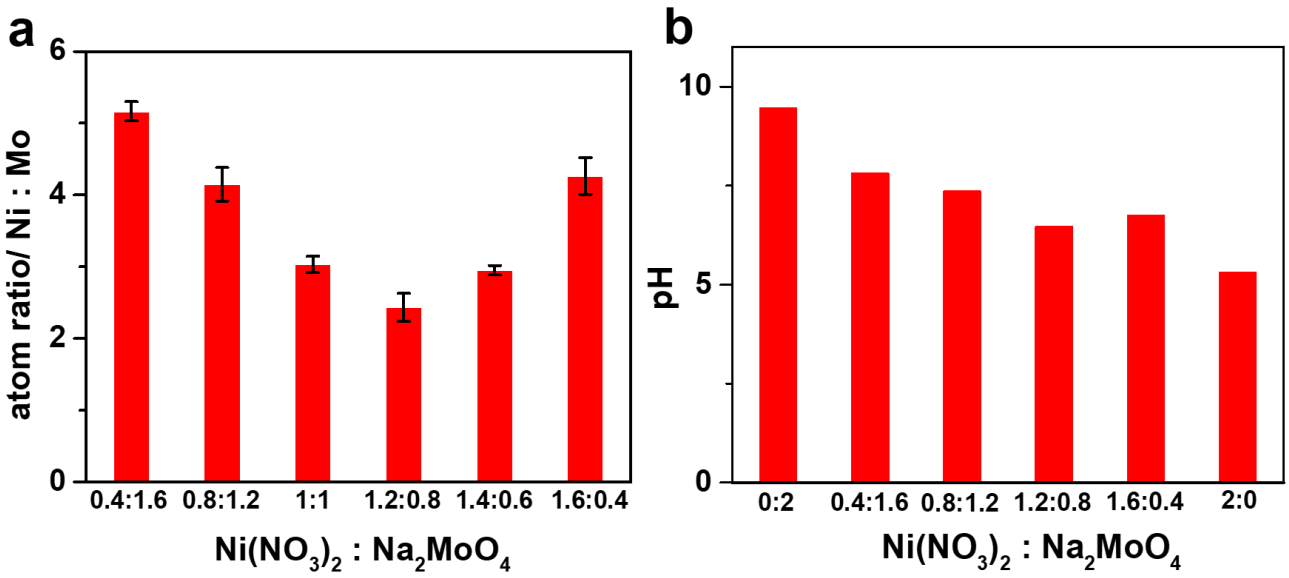

Fig. S3 (a) Ni:Mo atomic ratio and **(b)** pH of the solution before hydrothermal process with different feeding ratios (n mmol $Ni(NO_3)_2$ and m mmol Na_2MoO_4).

As the decrease of Na_2MoO_4 and increase of $Ni(NO_3)_2$ feeding amounts, the Ni: Mo atomic ratio firstly decreases but then goes up again. The lowest Ni:Mo ratio 2.44:1, which corresponds to the highest Mo content of 41at% relative to Ni, is obtained with 1.2 mmol $Ni(NO_3)_2$ and 0.8 mmol Na_2MoO_4. During the hydrothermal process, the pH value of the solution changes with the amount of Ni and Mo sources in **Fig. S3b**, and a mixture of $NiMoO_x$, NiO_x, MoO_x may be formed on the substrate, followed by sonication and rinsing. The Ni-Mo alloy is formed after hydrogen reduction treatment. The final step is electrochemical reduction at −0.52 V_{RHE} for 30 min in 1 M KOH, during which the remaining MoO_x is removed, and some metallic Mo may also be dissolved slightly. All these factors lead to variation of the final Ni:Mo ratio in the obtained catalyst.

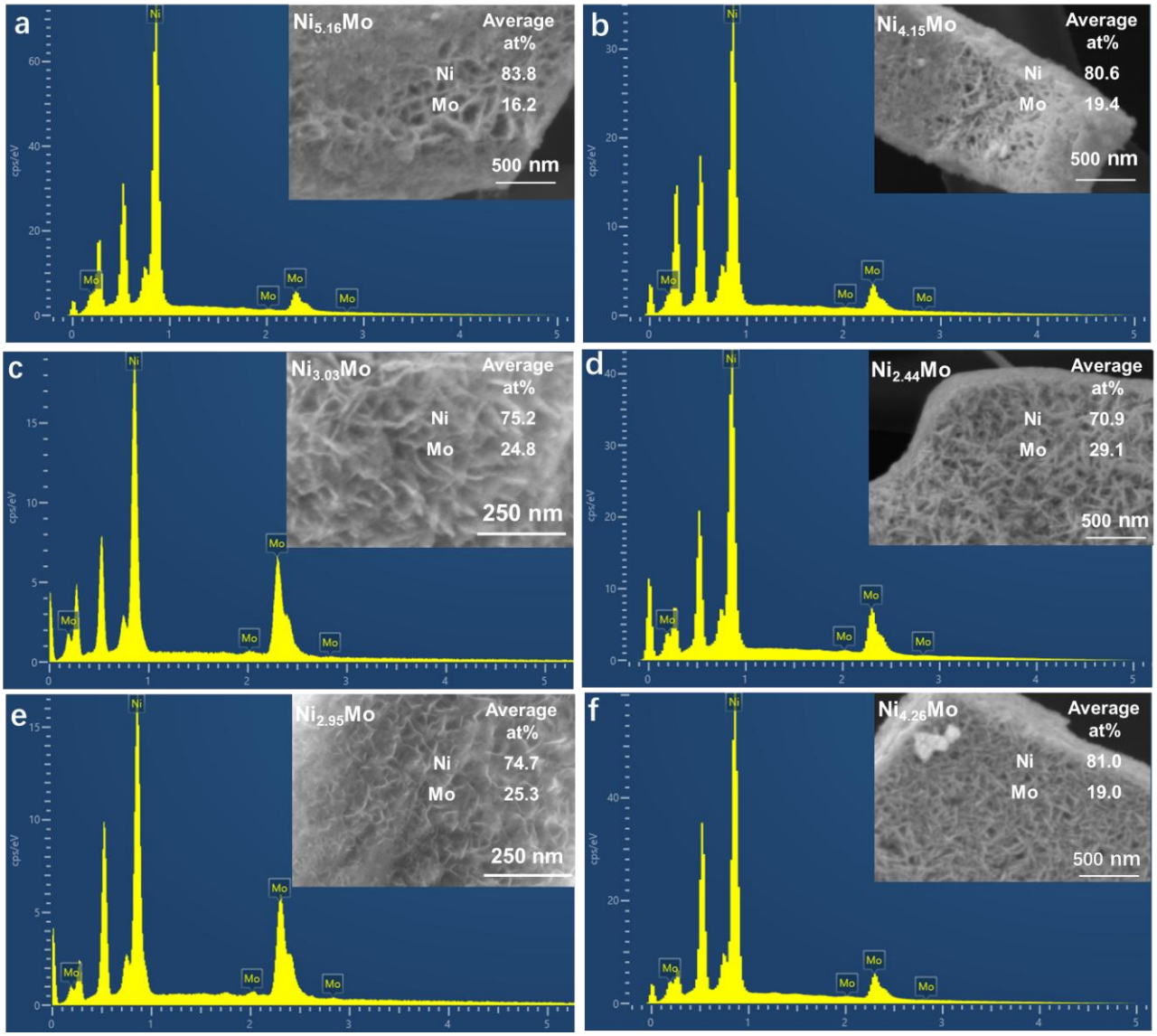

Fig. S4 The EDX spectra of **(a)** $Ni_{5.16}Mo$, **(b)** $Ni_{4.15}Mo$, **(c)** $Ni_{3.12}Mo$ **(d)** $Ni_{2.44}Mo$, **(e)** $Ni_{2.91}Mo$ and **(f)** $Ni_{4.26}Mo$ particles peeled off from the substrate. The insets are the corresponding SEM images and the average atomic percentage.

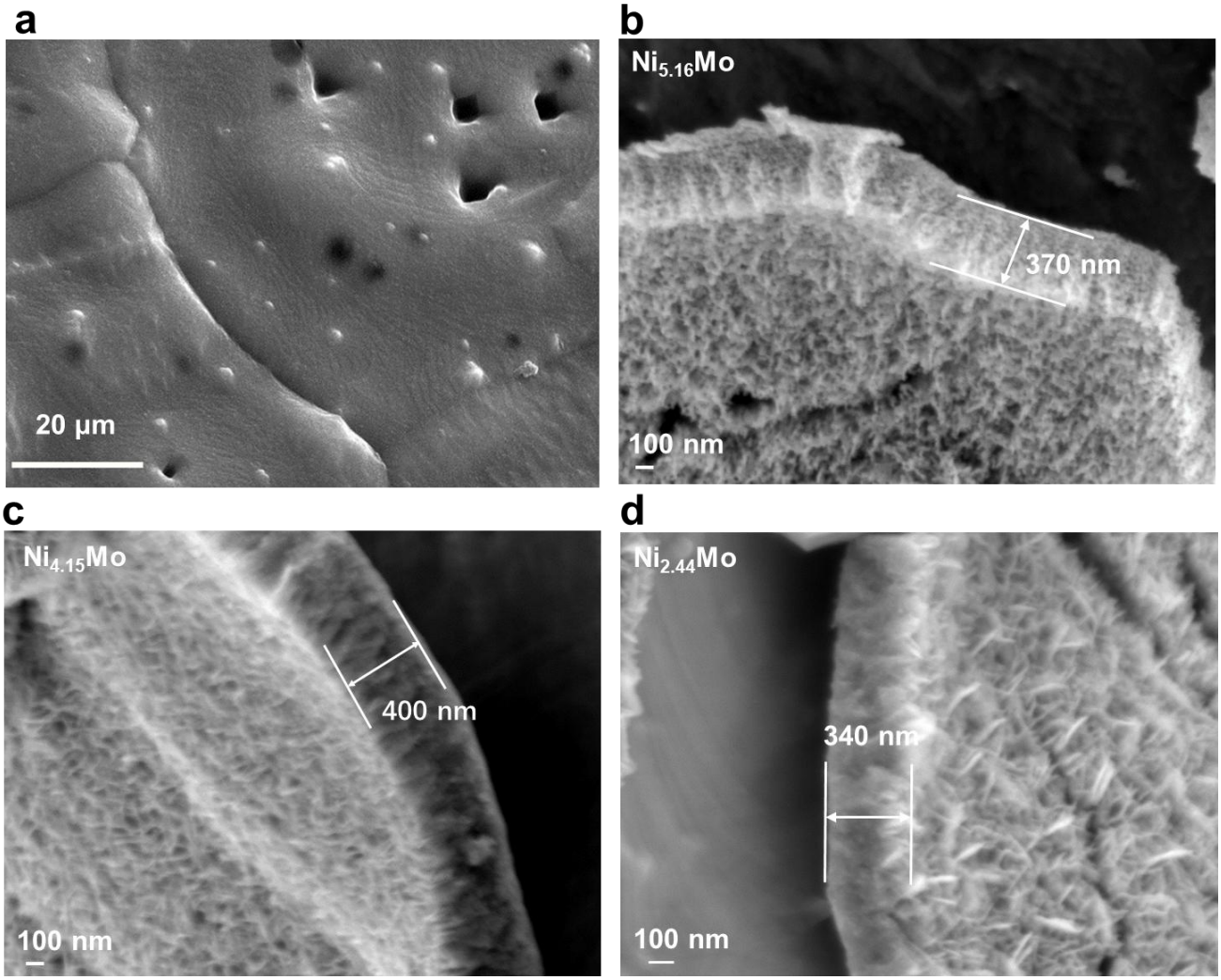

Fig. S5 (a) SEM image of Ni prepared similarly as Ni-Mo catalyst without adding Mo source**. (b-d)** The cross-section SEM images of Ni-Mo catalyst film peeled off from the substrate

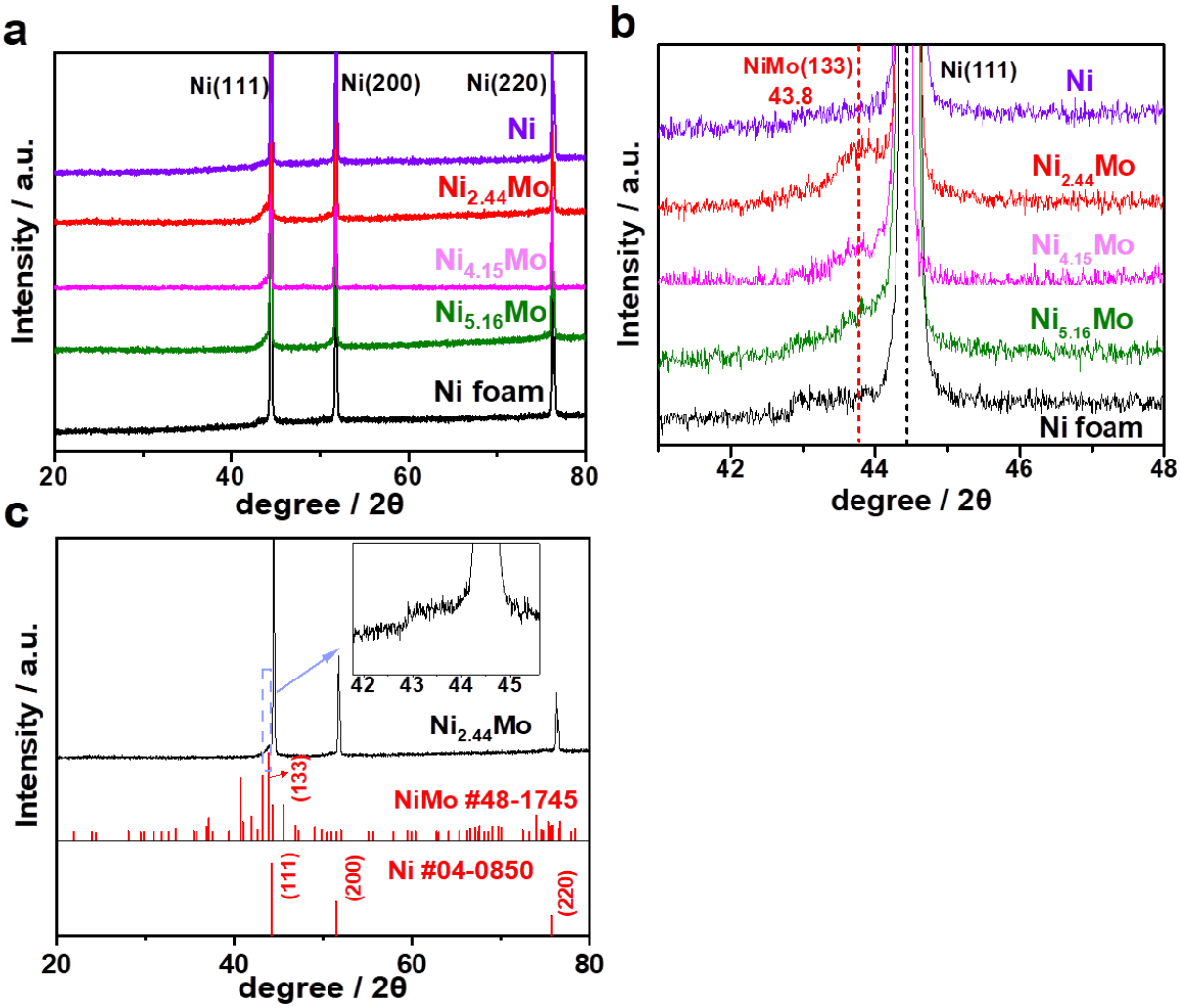

Fig. S6 X-ray diffraction (XRD) patterns of **(a, b)** various Ni-Mo catalysts and **(c)** $Ni_{2.44}Mo$ on Ni foams.

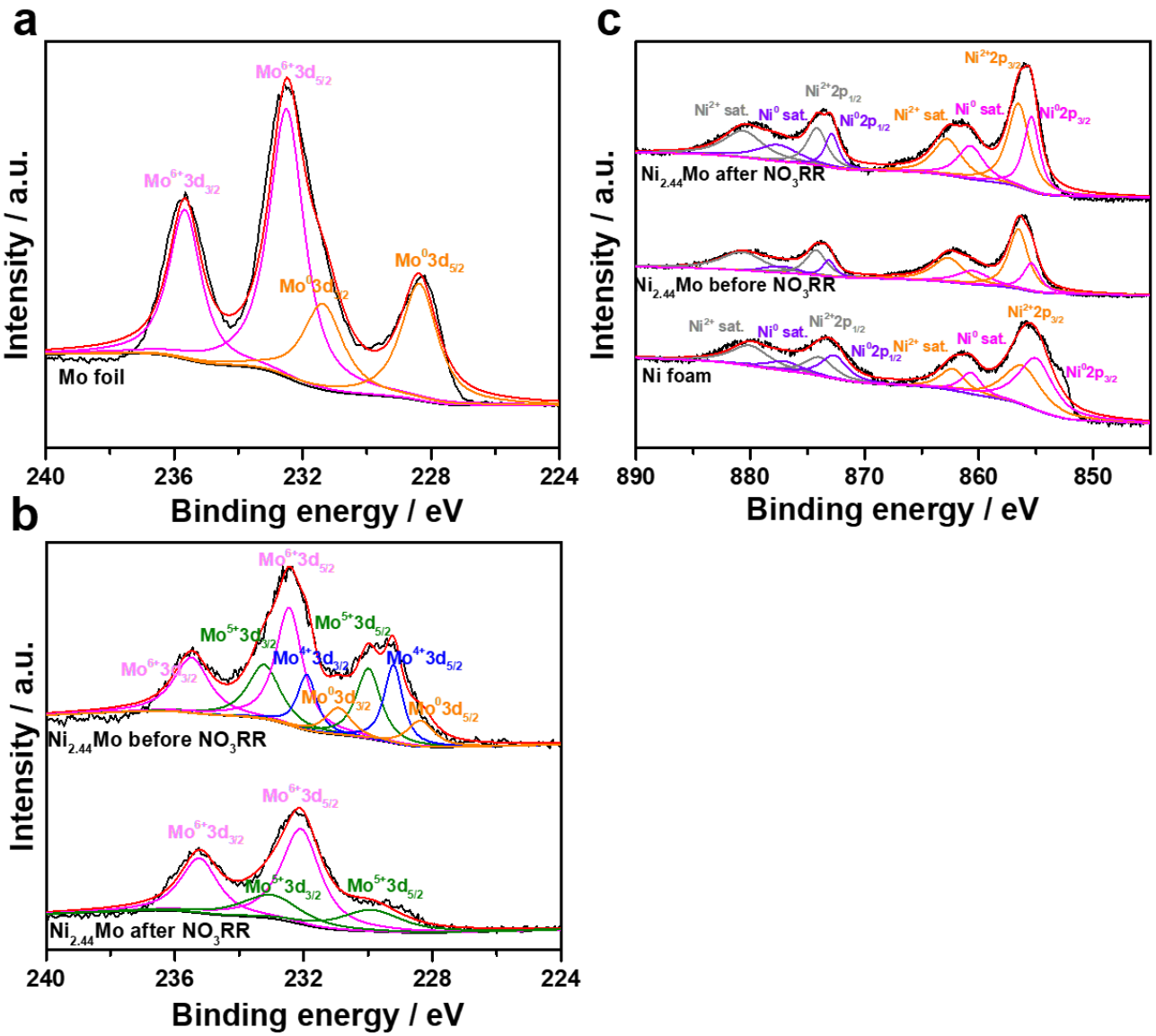

Fig. S7 The Mo 3d XPS spectra of **(a)** Mo foil, **(b)** $Ni_{2.44}Mo$ before and after NO_3RR. **(c)** The Ni 2p XPS spectra of Ni foam and $Ni_{2.44}Mo$ before and after NO_3RR.

Obvious signals of metallic Ni^0 and Mo^0 can be observed for $Ni_{2.44}Mo$ before NO_3RR. After NO_3RR, the metallic signals are obviously reduced. There are obvious Ni^{2+} and Mo^{6+} signals because the metallic nanoparticles are readily oxidized once exposed to air or alkaline solution without applying negative potential. These ex-situ XPS results cannot fullly reflect the real active species under NO_3RR conditions. The catalyst is prepared with H_2 reduction treatment at high temperature and electrochemical reduction treatment at very negative potential, thus metallic Ni-Mo species are most likely to be the active species during NO_3RR.

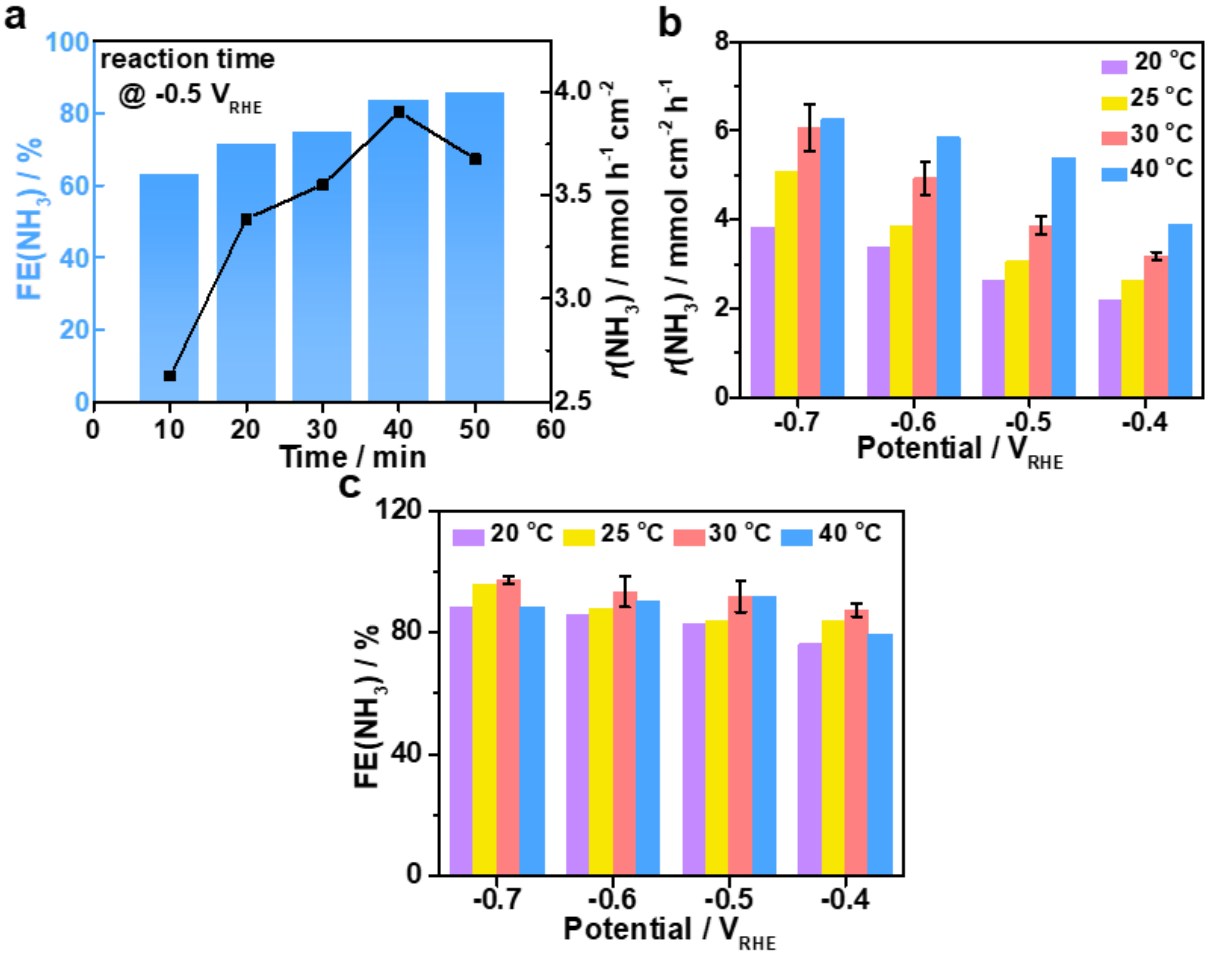

Fig. S8 Optimization of the NO_3RR conditions for $Ni_{2.44}Mo$. **(a)** Reaction time of NO_3RR. The **(b)** $r(NH_3)$ and **(c)** $FE(NH_3)$ at different temperatures of water bath.

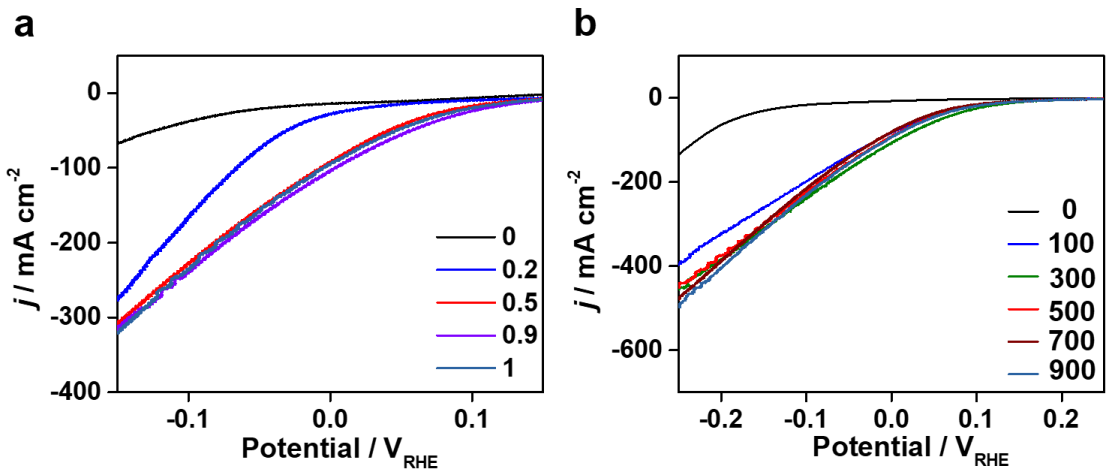

Fig. S9 LSV of $Ni_{2.44}Mo$ (**a**) under different $c(NO_3^-)$ (0, 0.2, 0.5, 0.9, 1 M) with 1 M of KOH, and (**b**) under different stirring rate (0, 100, 300, 500, 700, 900 rpm) with 0.5 M KNO_3 and 0.1 M KOH.

The LSV current density increases with the $c(NO_3^-)$ and stirring speed, and it reaches a steady state at 0.5 M NO_3^- and a stirring rate of 500 rpm, indicating mass diffusion effect can be neglected at this condition. Thus, a stirring rate of 500 rpm and concentration of 0.5 M KNO_3 was used for NO_3RR.

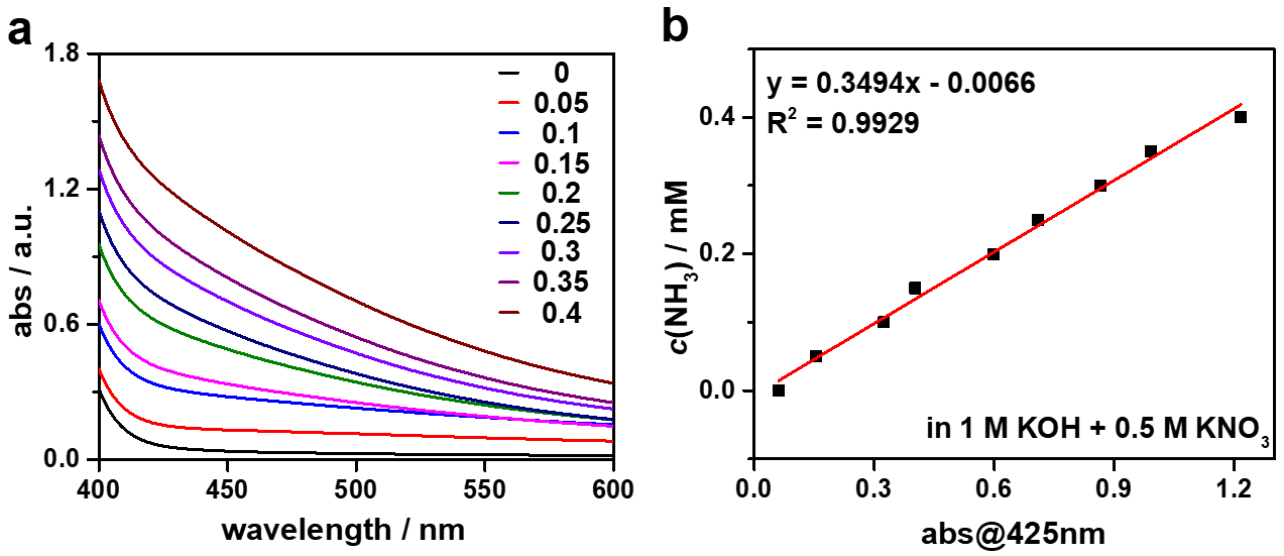

Fig. S10 (a) UV-vis spectra of Nessler reagent method using NH_4Cl solutions of different concentrations from 0 to 0.4 mM in 1 M KOH + 0.5 M KNO_3. **(b)** The standard curve used for the determination of NH_3 concentration.

The absorbance at 425 nm shows good linear relationship with NH_3 concentration.

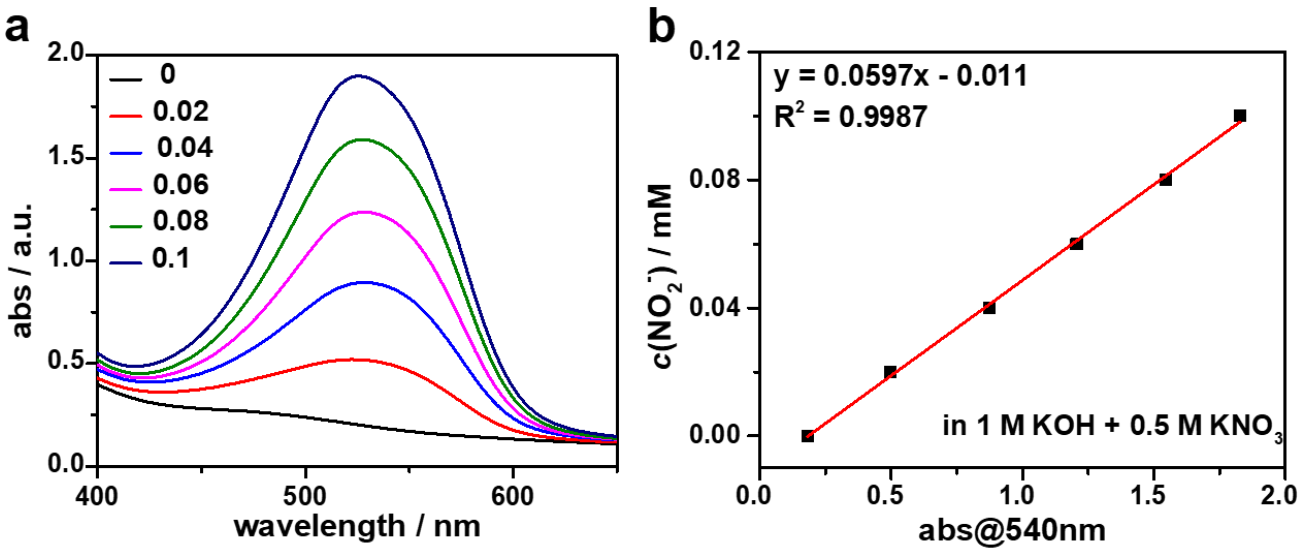

Fig. S11 (**a**) UV-vis spectra of Griess method using KNO_2 solutions of different concentrations from 0 to 0.1 mM in 1.0 M KOH + 0.5 M KNO_3. (**b**) The calibration curve used for estimation of NO_2^- concentration.

The absorbance at 540 nm shows good linear relationship with NH_3 concentration.

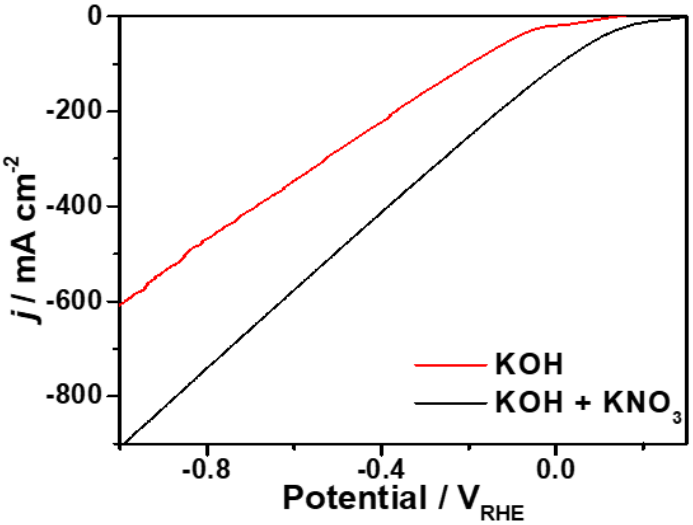

Fig. S12 LSV curves of $Ni_{2.44}Mo$ in 1 M KOH with/without 0.5 M KNO_3.

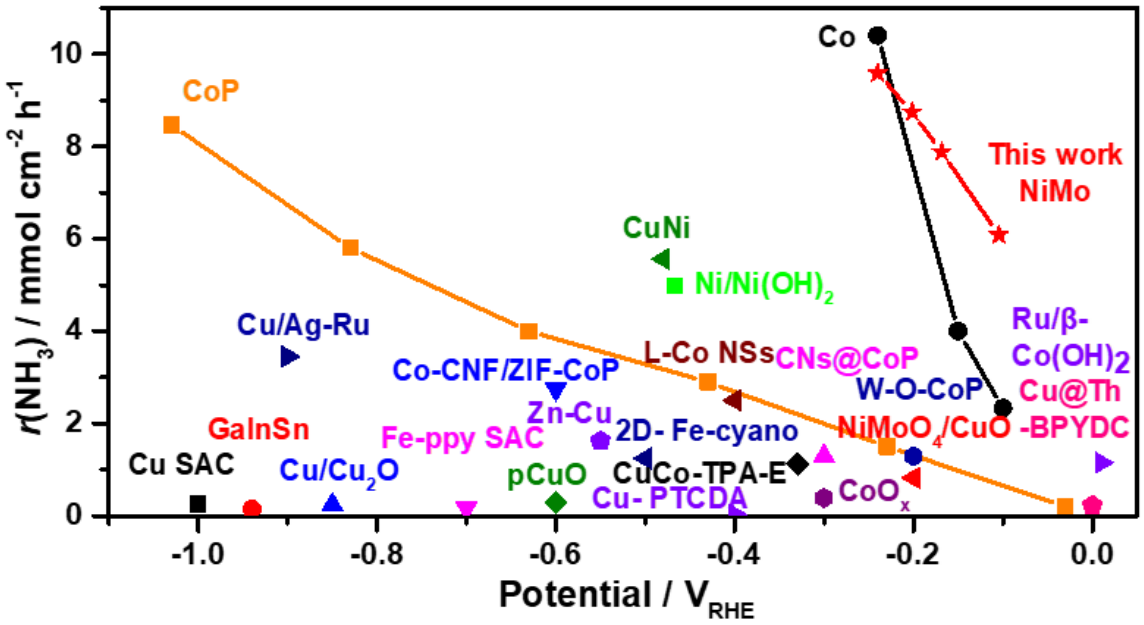

Fig. S13 Comparison of the electrocatalytic performance of $Ni_{2.44}Mo$ and those of other reported electrocatalysts for NO_3RR (details in **Table S2**).

Table S2 Comparison of the NH_3 production performances of $Ni_{2.44}Mo$ in this work with other reported NO_3RR electrocatalysts.

Electrocalalysts	Electrolyte	$r(NH_3)$ (mmol cm^{-2} h^{-1})	FE (%)	V_{RHE}	Ref. No.
$Ni_{2.44}Mo$	**0.5 M KNO_3 + 1 M KOH**	**6.08**	**97**	**−0.1**	**This work**
CoP	1 M $NaNO_3$ + 1 M NaOH	8.47	88.6	−1.03[a]	13
Cu-N-C SAC	0.1 M KNO_3 + 0.1 M KOH	0.26	84.7	−1[a]	14
GaInSn	0.1 M HNO_3	0.14	~95	−0.94	15
Cu/Cu_2O NWAs	200 ppm NO_3^- + 0.5 M Na_2SO_4	0.24	95.8	−0.85	16
Fe-PPy SACs	0.1 M KNO_3 + 0.1 M KOH	0.16	98	−0.7	17
pCuO-5	0.05 M KNO_3 + 0.05 M H_2SO_4	0.29	80	−0.6	18
2D Fe-cyano nanosheets	0.1 M KNO_3 + 1 M KOH	1.24	90.4	−0.5	19
Cu-incorporated-PTCDA	500 ppm NO_3^- + 0.1 M PBS	0.03	85.9	−0.4	20
CoO_x	0.1 M KOH + 0.1 M KNO_3	0.39	93.4	−0.3	21
Co nanoarrays	0.1 M KNO_3 +0.5 M K_2SO_4	10.4	~97	−0.24	22
Cu@Th-BPYDC	0.1 M KNO_3 + 1 M KOH	0.23	92.5	0	23

Zn-Cu	0.1 M KNO_3 +0.5 M K_2SO_4	1.62	80	-0.55	24
CuNi	0.71 M KNO_3 + 1 M KOH	5.56	97	-0.48[a]	25
W-O-CoP	0.1 M $NaNO_3$ + 1 M KOH	1.29	95.2	-0.2[a]	26
CNs@CoP	0.1 M $NaNO_3$ +1 M KOH	1.3	96.2	-0.3[a]	27
Ru/β-$Co(OH)_2$	0.1 M KNO_3 + 1 M KOH	1.15	95.1	0.01	28
Ni/$Ni(OH)_2$	0.5 M KNO_3 + 1 M KOH	4.98	98.5	-0.467	29
$NiMoO_4$/CuO	0.05 M KNO_3 + 1 M KOH	0.82	98.8	-0.2	30
Co-CNF/ZIF-CoP	0.1 M KNO_3 + 1 M KOH	2.74	96.8	-0.6	31
CuCo-TPA-E	0.1 M KNO_3 + 1 M KOH	1.12	99.6	-0.33	32
L-Co NSs	0.05 M KNO_3 + 1 M KOH	2.5	98.6	-0.4	33
Cu/Ag-Ru	0.1 M KNO_3 + 1 M KOH	3.45	94.93	-0.9	34

Note:

[a] The superscript indicates the applied potential was not corrected by *iR* drop. Otherwise mentioned, the potential was *iR*-corrected.

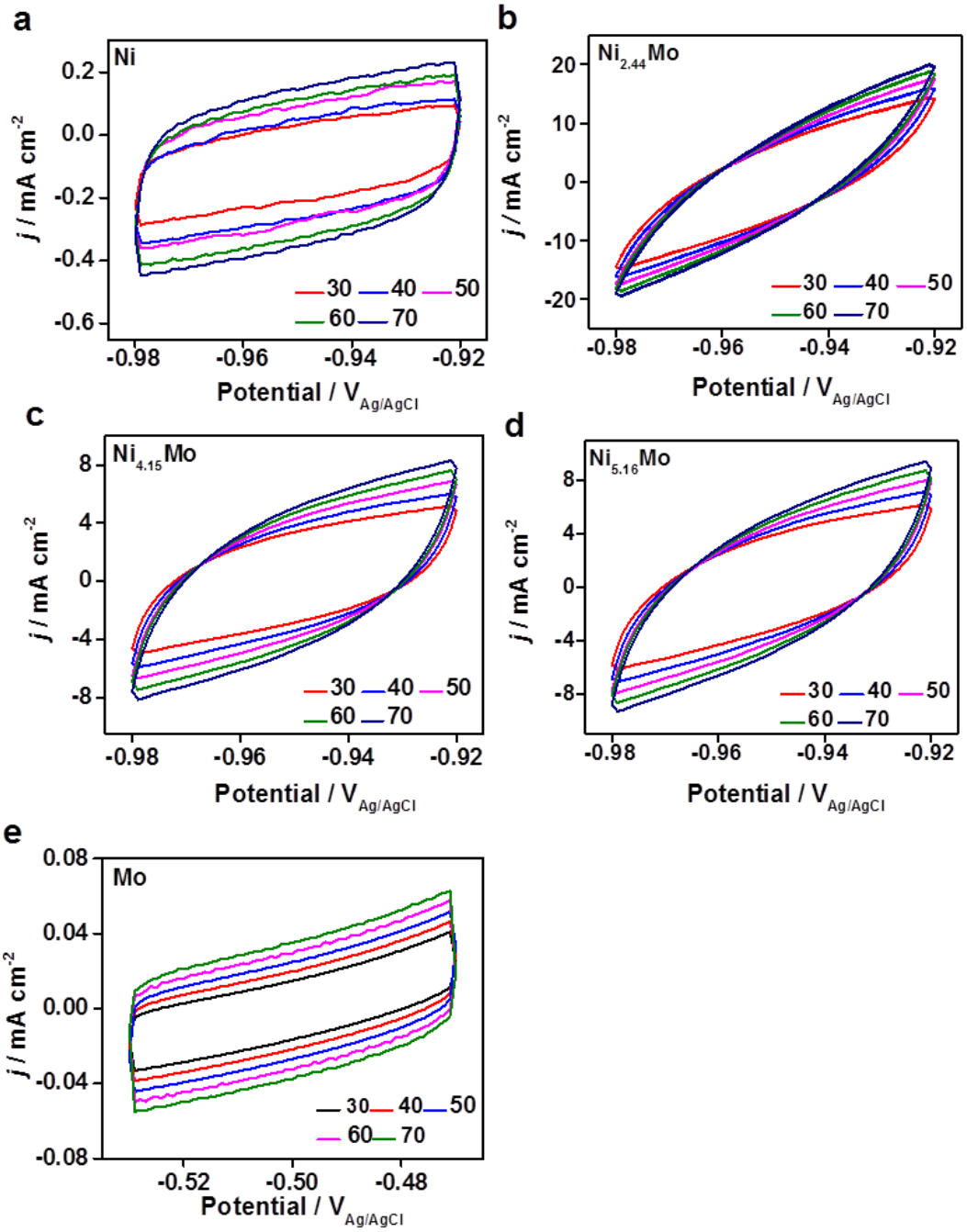

Fig. S14 CV curves of **(a)** Ni, **(b)** $Ni_{2.44}Mo$, **(c)** $Ni_{4.15}Mo$, **(d)** $Ni_{5.16}Mo$, and **(e)** the Mo foil in 1 M KOH with different scan rates of 30, 40, 50, 60, and 70 mV/s.

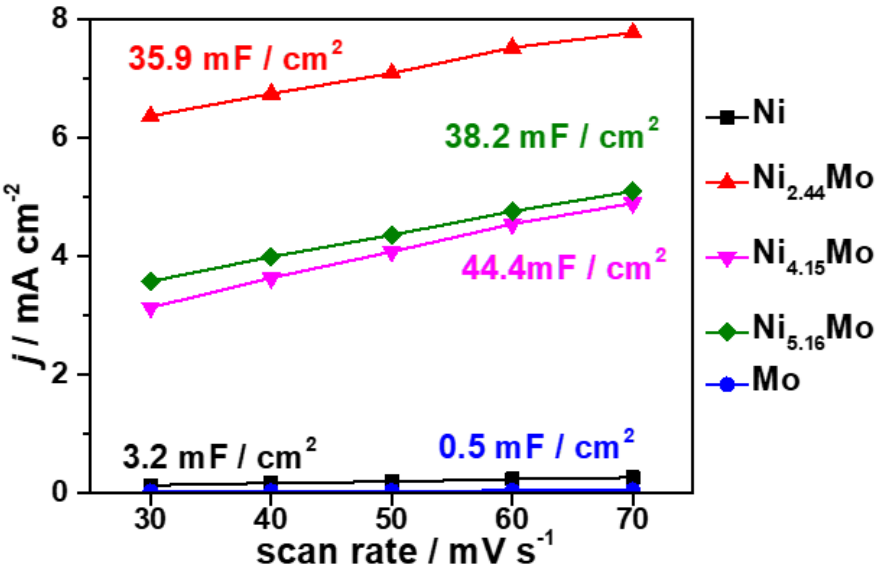

Fig. S15 ECSA of different Ni-Mo catalysts in 1 M KOH**.**

Supposing the area of a Mo foil is 1 cm^2, the ECSAs of Ni, $Ni_{2.44}Mo$, $Ni_{4.15}Mo$, and $Ni_{5.16}Mo$ electrodes are 6.4, 71.8, 88.8, and 76.4 cm^2, respectively.

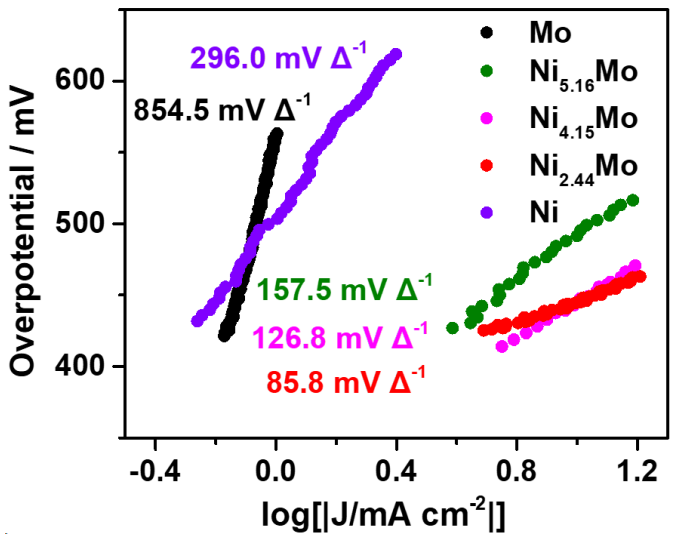

Fig. S16 Tafel slopes of $Ni_{5.16}Mo$, $Ni_{4.15}Mo$, $Ni_{2.44}Mo$, Ni foam and Ni in 1 M KOH + 0.5 M KNO_3 measured under a scan rate of 10 mV/s with 80% *iR* compensation.

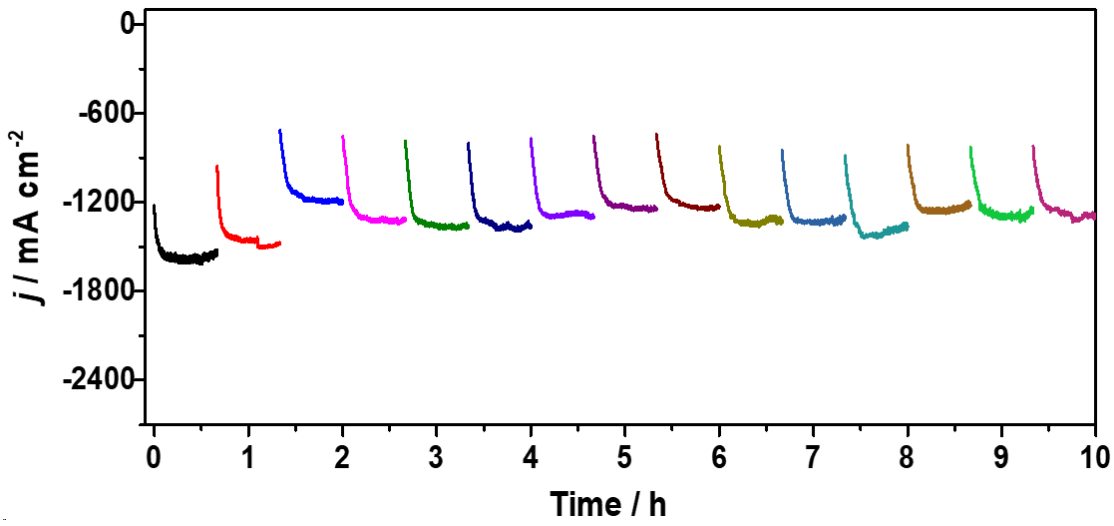

Fig. S17 Current density over $Ni_{2.44}Mo$ catalyst during 15 cycles of stability tests (40 min for each cycle). Electrode area: 0.6*0.6 cm^2. Conditions: 10 mL of mixed solution of KOH (1 M) and KNO_3 (0.5 M) in 30 ºC water bath under 500 rpm at −0.7 V_{RHE} without *iR* compensation.

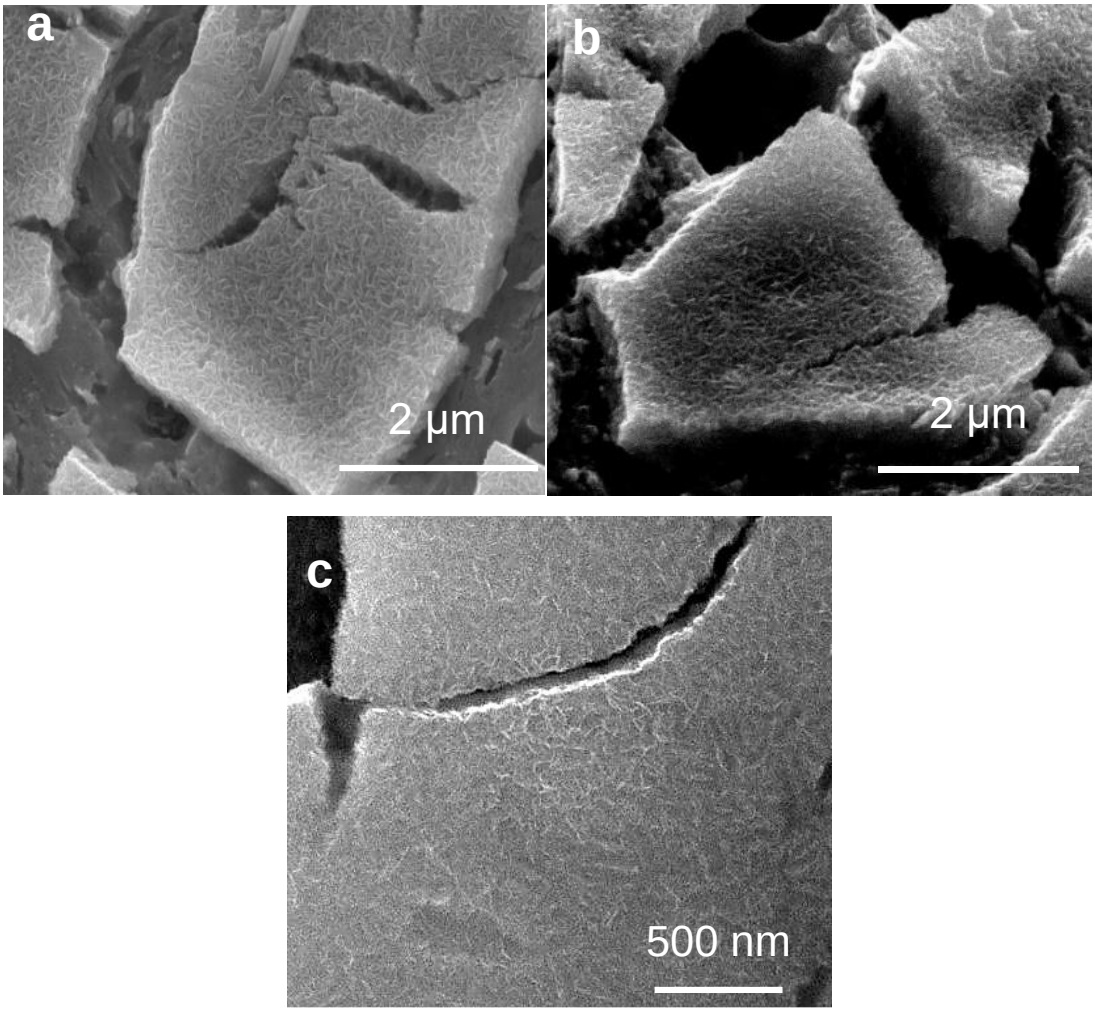

Fig. S18 SEM images of $Ni_{2.44}Mo$ **(a)** before pretreatment, **(b)** after pretreatment, and **(c)** after NO_3RR.

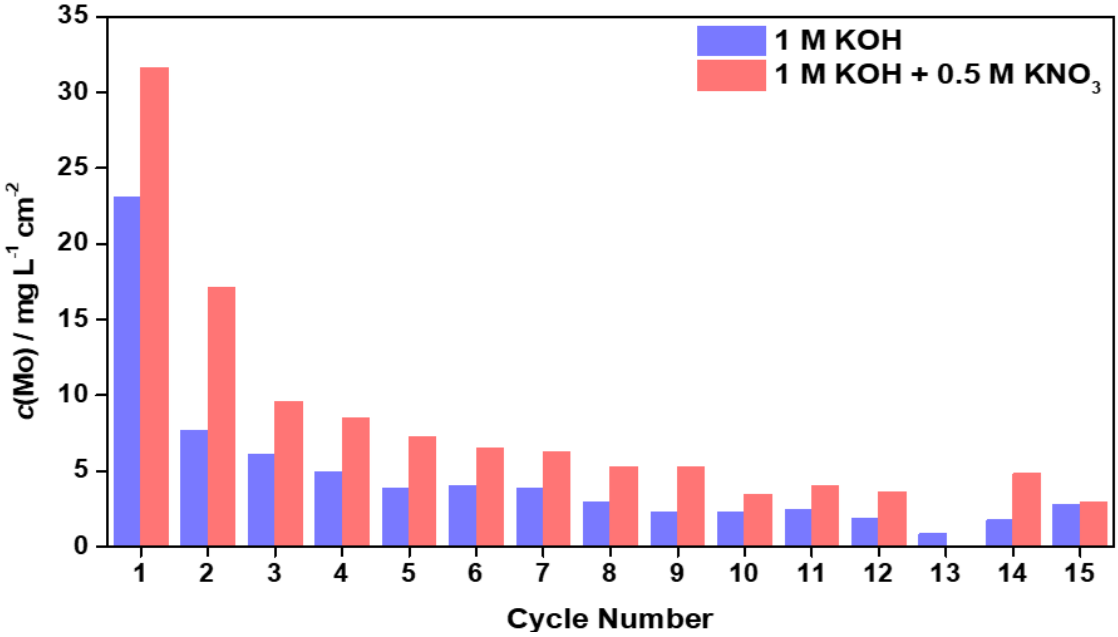

Fig. S19 Dissolution of Mo from $Ni_{2.44}Mo$ catalyst into the electrolyte under 15 cyclic stability tests (40 min for each cycle). Reaction conditions: electrode area was fixed to 0.36 cm^2, with 10 mL of mixed solution of KOH (1 M) and KNO_3 (0, 0.5 M) in 30 ºC water bath under 500 rpm at −0.7 V_{RHE} without *iR* compensation.

There is slight dissolution of Mo species into the electrolyte whether there is NO_3^- (mainly occurs NO_3RR) or not (mainly occurs hydrogen evolution reaction). The rate of dissolution declines obviously as a function of time. It is inferred that an equilibrium of dissolution and re-deposition under negative potential may be established after long time reaction.

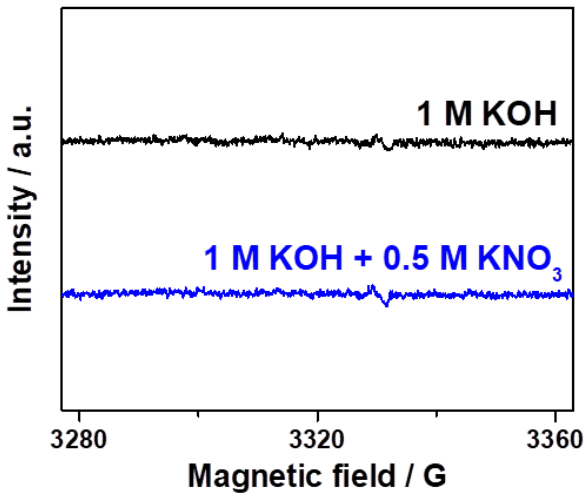

Fig. S20 EPR spectra of electrolyte (1 M KOH and 1 M KOH + 0.5 M KNO_3) without electrolysis using DMPO as the radical trapping reagent.

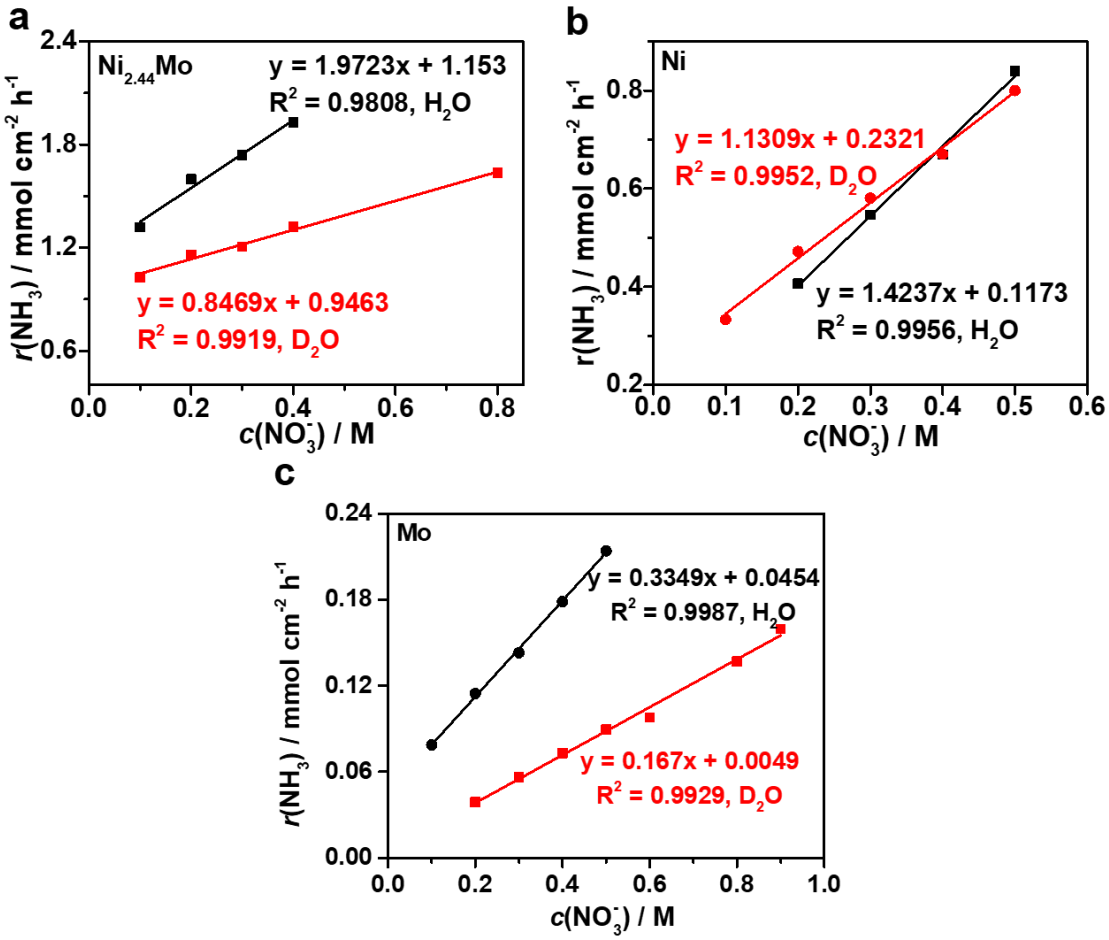

Fig. S21 KIE tests in H_2O and D_2O. (a) $Ni_{2.44}Mo$, **(b)** Ni, and **(c)** Mo in 1 M KOH with different $c(NO_3^-)$.

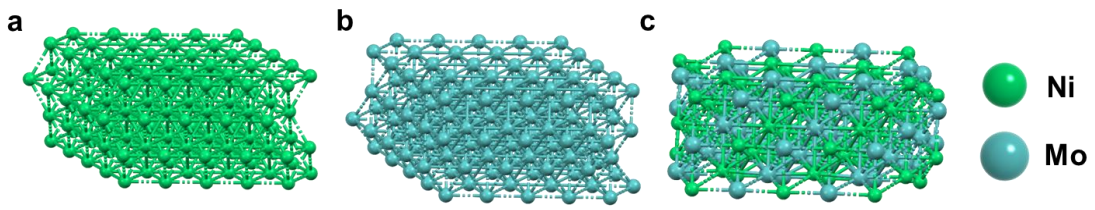

Fig. S22 The atom configurations of **(a)** Ni (111), **(b)** Mo (111) and **(c)** NiMo (133)

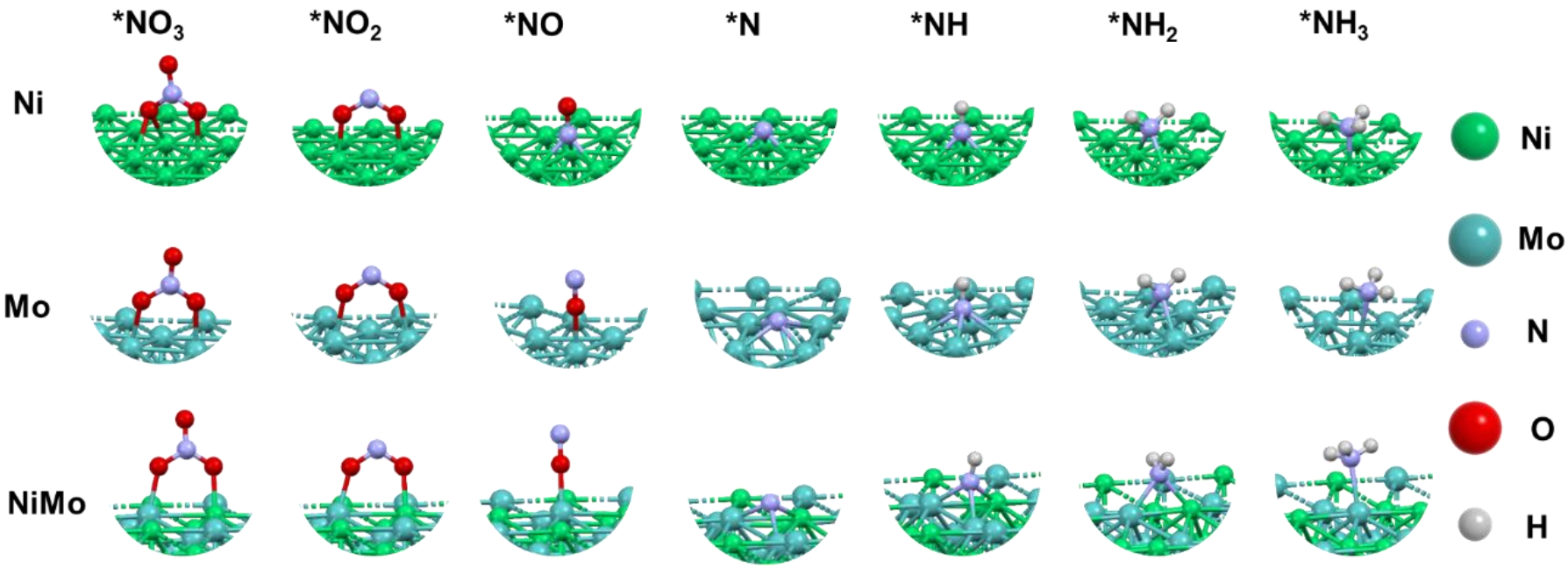

Fig. S23 The most stable adsorption configurations of different intermediates for NO_3RR on Ni (111), Mo (111) and NiMo (133)**.**

Supplementary References

1. Y. Zhao, F. Wu, Y. Miao, C. Zhou, N. Xu, R. Shi, L.-Z. Wu, J. Tang and T. Zhang, Angew. *Chem. Int. Ed.*, 2021, **40**, 60, 21728-21731.
2. G.-F. Chen, Y. Yuan, H. Jiang, S.-Y. Ren, L.-X. Ding, L. Ma, T. Wu, J. Lu and H. Wang, *Nat. Energy*, 2020, **8**, 5, 605-613.
3. G. Kresse, J. Furthmiiller, *Phys. Rev. B*, 1996, **54**, 16, 11169.
4. G. Kresse, J. Furthmiiller, *Comput. Mater. Sci*, 1996, **6**, 15-50.
5. P. E. Blochl, *Phys. Rev. B*, 1994, **50**, 24, 17953.
6. G. Kresse and D. Joubert, *Phys. Rev. B*, 1999, **59**, 3, 1758.
7. J. P. Perdew, K. Burke and M. Ernzerhof, *Phys. Rev. Lett.*, 1996, **77**, 18, 3865.
8. S. Grimme, J. Antony, S. Ehrlich and H. Krieg, *J. Chem. Phys.*, 2010, **132**, 154104.
9. G. Henkelman, B. P. Uberuaga and H. Jo´nsson, *J. Chem. Phys.*, 2000, **113**, 9901.
10. J. K. Nørskov, J. Rossmeisl, A. Logadottir and L. Lindqvist, *J. Phys. Chem. B*, 2004, **108**, 17886-1789.
11. V. Wang, N. Xu, J.-C. Liu, G. Tang and W.-T. Geng, *Comput. Phys. Commun.*, 2021, **267**, 108033.
12. Y. Fu, S. Wang, Y. Wang, P. Wei, J. Shao, T. Liu, G. Wang and X. Bao, *Angew. Chem. Int. Ed.*, 2023, **62**, e202303327.
13. K. Fan, W. Xie, J. Li, Y. Sun, P. Xu, Y. Tang, Z. Li and M. Shao, *Nat. Commun.*, 2022, **13**, 7958−7970.
14. J. Yang, H. Qi, A. Li, X. Liu, X. Yang, S. Zhang, Q. Zhao, Q. Jiang, Y. Su, L. Zhang, J. Li, Z. Tian, W. Liu, A. Wang and T. Zhang, *J. Am. Chem. Soc.*, 2022, **144**, 12062−1207.
15. J. Crawford, H. Yin, A. Du and A. P. O'Mullane, *Angew. Chem. Int. Ed.*, 2022, **61**,

e202201604.

16. Y. Wang, W. Zhou, R. Jia, Y. Yu and B. Zhang, *Angew. Chem. Int. Ed.*, 2020, **59**, 5350−5354.
17. P. Li, Z. Jin, Z. Fang and G. Yu, *Energy Environ. Sci.*, 2021, **14**, 3522–3531.
18. R. Daiyan, T. Tran-Phu, P. Kumar, K. Iputera, Z. Tong, J. Leverett, M. H. A. Khan, A. A. Esmailpour, A. Jalili, M. Lim, A. Tricoli, R.S. Liu, X. Y. Lu, E. Lovell and R. Ama, *Energy Environ. Sci.*, 2021, **14**, 3588-3598.
19. Z. Fang, Z. Jin, S. Tang, P. Li, P. Wu and G. Yu, *ACS Nano*, 2022, **16**, 1072−1081.
20. G.-F. Chen, Y. Yuan, H. Jiang, S.-Y. Ren, L.-X. Ding, L. Ma, T. Wu, J. Lu and H. Wang, *Nat. Energy*, 2020, **5**, 605−613.
21. J. Wang, C. Cai, Y. Wang, X. Yang, D. Wu, Y. Zhu, M. Li, M. Gu and M. Shao, *ACS Catal.*, 2021, **11**, 15135−15140.
22. X. Deng, Y. Yang, L. Wang, X.-Z. Fu and J.-L. Luo, *Adv. Sci.*, 2021, **8**, 2004523−2004531.
23. Z. Gao, Y. Lai, Y. Tao, L. Xiao, L. Zhang and F. Luo, *ACS Cent. Sci.*, 2021, **7**, 1066−1072.
24. L. Wu, J. Feng, L. Zhang, S. Jia, X. Song, Q. Zhu, X. Kang, X. Xing, X. Sun and B. Han, *Angew. Chem. Int. Ed.*, 2023, **62**, e202307952.
25. W. Yu, J. Yu, M. Huang, Y. Wang, Y. Wang, J. Li, H. Liu and W. Zhou, *Energy Environ. Sci.*, 2023, **16**, 2991-3001.
26. Z. Chang, G. Meng, Y. Chen, C. Chen, S. Han, P. Wu, L. Zhu, H. Tian, F. Kong, M. Wang, X. Cui and J. Shi, *Adv. Mater.*,2023, **35**, 2304508**.**
27. J. Li, H. Li, K. Fan, J. Y. Lee, W. Xie and M. Shao, *Chem Catal.*, 2023, **3**, 100638**.**
28. W. Zhu, F. Yao, Q. Wu, Q. Jiang, J. Wang, Z. Wang and H. Liang, *Energy Environ. Sci.*, 2023, **16**, 2483-2493.

29. X. Shi, M. Xie, K. Yang, Y. Niu, H. Ma, Y. Zhu, J. Li, T. Pan, X. Zhou, Y. Cui, Z. Li, Y. Yu, X. Yu, J. Ma and H. Cheng, *Angew. Chem. Int. Ed.*, 2024, **63**, e202406750**.**
30. C. Lin, X. Chen, L. Wang, W. Li, Z. Wang, M. Li, J. Feng, B. Hou and W. Yan, *Adv. Funct. Mater.*, 2024, **34**, 2401287**.**
31. R. Qi, Z. Wang, M. Zhong, C. Wang, F. Bai and X. Lu, *Small*, 2024, **20**, 2308311**.**
32. J. Yang, W.-D. Zhang, H. Zhao, Y. Zou, Z.-Y. Zhang, J. Liu, J. Wang, Z.-G. Gu and X. Yan, *Appl. Catal. B-Environ.*, 2024, **340**, 123237**.**
33. W. Sun, Y. Xu, L. Yang, W. Wen, H. Zhang and X.-Y. Yu, *Small*, 2025, **21**, 2411215.
34. R. Jia, X. Zhang, L. Gan, M. Tahir, Z.-F. Huang, L. Pan, R. Gao, C. Shi, X. Zhang, G. Yang and J.-J. Zou, *J. Mater. Chem. A*, 2025, **13**, 5732–5743.